Solar Phys (2013) 288:1–22
DOI 10.1007/s11207-012-0147-x

INITIAL RESULTS FROM FISS

Fast Imaging Solar Spectrograph of the 1.6 Meter New Solar Telescope at Big Bear Solar Observatory

Jongchul Chae · Hyung-Min Park · Kwangsu Ahn · Heesu Yang · Young-Deuk Park · Jakyoung Nah · Bi Ho Jang · Kyung-Suk Cho · Wenda Cao · Philip R. Goode

Received: 8 April 2012 / Accepted: 24 September 2012 / Published online: 23 October 2012

Abstract For high resolution spectral observations of the Sun – particularly its chromosphere, we have developed a dual-band echelle spectrograph named Fast Imaging Solar Spectrograph (FISS), and installed it in a vertical optical table in the Coudé Lab of the 1.6 meter New Solar Telescope at Big Bear Solar Observatory. This instrument can cover any part of the visible and near-infrared spectrum, but it usually records the Hα band and the Ca II 8542 Å band simultaneously using two CCD cameras, producing data well suited for the study of the structure and dynamics of the chromosphere and filaments/prominences. The instrument does imaging of high quality using a fast scan of the slit across the field of view with the aid of adaptive optics. We describe its design, specifics, and performance as well as data processing

Keywords Chromosphere · Instrumentation and data management · Spectrum, visible

1. Introduction

The chromosphere is a layer of the solar atmosphere that is still poorly understood despite its importance in connecting the high-β photosphere and the low-β corona (Judge, 2006). Even though often assumed to be a hydrostatic, plane-parallel layer, the chromosphere is obviously neither hydrostatic, nor plane-parallel, and comprises a variety of inhomogeneous features that are magnetically supported against gravity and/or often move fast

---

Initial Results from FISS
Guest Editor: Jongchul Chae

J. Chae (✉) · H.-M. Park · H. Yang
Department of Physics and Astronomy, Seoul National University, Seoul, 151-747, Korea
e-mail: chae@astro.snu.ac.kr

Y.-D. Park · J. Nah · B.H. Jang · K.-S. Cho
Korea Astronomy and Space Science Institute, Daejeon, Korea

K. Ahn · W. Cao · P.R. Goode
Big Bear Solar Observatory, New Jersey Institute of Technology, 40386 North Shore Lane, Big Bear City, CA 92314, USA

(Rutten, 2006). It appears that a proper understanding of the chromosphere critically depends on the investigation of these features. Since these chromospheric features are usually fine-structured (down to 0.2″ or below) and short-lived (a few 10 s or shorter), and often move at high speeds (Reardon, Uitenbroek, and Cauzzi, 2009), the study of their structures, dynamics, and energetics requires imaging spectroscopy of high spectral resolution, high spatial resolution, and high temporal resolution.

One way to do imaging spectroscopy is to take a series of monochromatic images, at a number of wavelengths using a tunable filter, within a short time. In the past a tunable birefringent filter was usually used (*e.g.* Chae, Park, and Park, 2006), but now a Fabry–Pérot interferometer is preferred because of its fast tuning capability and high transmission. The imaging spectroscopy based on a Fabry–Pérot interferometer is particularly attractive in that it can do excellent imaging with a spatial resolution as high as the diffraction-limited one with the help of image processing techniques such as speckle reconstruction. The Interferometric BIdimensional Spectrometer (IBIS) of the Dunn Solar Telescope is a well-operating instrument of this kind (Cavallini, 2006). The shortcomings of this technique are the narrow free spectral range and a finite duration needed to scan a spectral line, which may make it difficult to observe high-speed features and fast-changing features, respectively.

One can do imaging spectroscopy as well by taking a series of spectrograms using a grating-spectrograph with successively changing the position of the slit across the field of view. Many instruments of this kind have been constructed, including the high-speed video spectroheliograph of the 60 cm Domeless Solar Telescope at Hida Observatory (Hanaoka, 2003). Currently this technique is not much favored since its imaging capability is poorer than the filter-based imaging spectroscopy. In contrast with the filter-based imaging spectroscopy, there is no good way to process data taken by a spectrograph to overcome the seeing problem, a big obstacle to the performance of imaging instruments on ground. For high quality imaging, the light fed into the spectrograph should be free from such troublesome seeing. Either the instrument has to be put in space or the incident light should be corrected for the seeing by, for instance, adaptive optics. Since the technology of adaptive optics is developing rapidly in solar observations, it appears that the spectrograph-based imaging spectroscopy will have satisfactory imaging capability in the near future.

The greatest advantage of a spectrograph-based imaging spectroscopy is obviously that the acquired data are primarily spectral (Hanaoka, 2003) so that it is not required to reconstruct data to obtain spectral profiles. Thus this kind of imaging spectroscopy is quite suited for the spectral study of high-speed or fast-changing features. Moreover, its wide free spectral range allows each spectrum to contain not only very strong lines, suited for the study of the chromosphere, but also weak lines and continuum, useful for the study of the photosphere, so that it becomes a straightforward task to co-align a chromospheric feature and a photospheric feature at the same location on the Sun.

A recent development in imaging spectroscopy is the integral field spectroscopy (IFS) that simultaneously takes the spectra at a number of points that correspond to image pixels in the field of view, usually with the help of fibers. This is a true three-dimensional spectroscopy in that both imaging information and spectral information are acquired simultaneously. The field of view of a typical IFS is small, but may be more suitable for study of the small-scale dynamic chromosphere revealed by *Hinode* (*e.g.* Shibata *et al.*, 2007; de Pontieu *et al.*, 2007) and other advanced ground-based telescopes (*e.g.* Langangen *et al.*, 2008), and also met with a small iso-planatic patch corrected by adaptive optics on the ground. In covering a large field of view, however, an image-scanning slit spectrograph described above may excel.

We have developed a dual-band echelle spectrograph with imaging capability, named the Fast Imaging Solar Spectrograph (FISS). This instrument was installed on a vertical table in the Coudé Lab of the 1.6 meter New Solar Telescope at Big Bear Solar Observatory (Goode *et al.*, 2003, 2010; Cao *et al.*, 2010). In this paper, we describe its concepts, details, data processing, and the performance of the early runs. More technical details and test results obtained in the development stage were previously reported by Nah *et al.* (2011) and Park (2011).

2. Basic Concepts of the FISS Design

2.1. Scientific Objectives

The major objective of the FISS is to investigate the structure and dynamics of plasma in the chromospheric features. Particularly we expect to obtain observational data which can help us in finding answers to important scientific questions such as: what is the basic mechanism of non-hydrostatic support of plasma in the chromosphere? What are the building blocks of the chromosphere? Stratified layers? Thin threads? Jet-like features? Clouds? What are the thermodynamic and dynamics properties of these features? What criteria can be used to classify a variety of jet-like features into distinct types? Which types are driven by the process of magnetic reconnection and which types are not? Is magnetic reconnection in the photosphere and chromosphere important in the heating of the chromosphere? How important are waves and shocks? How is the chromosphere dynamically and thermally linked to the photosphere and to the corona?

2.2. Concepts of Design

Our strategy to achieve these scientific objectives is to acquire observational data that can be used to determine the physical parameters – such as line-of-sight velocity, temperature, non-thermal motion, and, hopefully, electron density – of each chromospheric feature with high spatial resolution and high temporal resolution. With this strategy in mind, we have designed FISS with the following concepts. First, the FISS uses an echelle grating as the main spectral element with the aid of interference filters for the order sorting. Our adoption of this element naturally makes spectrograms – spectral-spatial maps of intensity – be the basic data to be obtained by the instrument.

Second, the instrument is able to record a properly chosen pair of two spectral bands simultaneously. This adds extra spectral information that sometimes turns out to be invaluable in the determination of physical parameters. For example, the combination of Doppler absorption width of hydrogen lines and that of Ca II lines can be used to determine temperature and non-thermal motion separately because of the difference in the atomic weight between hydrogen and calcium. This unique diagnostic is effective especially in a plasma structure – such as fibrils and prominences – that lies high above the background chromosphere and contain neutral hydrogen atoms and Ca II ions numerous enough to significantly affect both line profiles. In this kind of cloud-like structures, it is possible to distinguish the effect of the structure – such as Doppler broadening – on the observed line profiles from that of the background chromosphere with the help of a simple model of radiative transfer such as the cloud model (Beckers, 1964; Tziotziou, 2007).

Third, the instrument does imaging based on the fast scan of the slit across the field of view. This function is indispensable to the spatial identification of features. Since features may change with time, the scan should be done as fast as possible.

2.3. Data Requirement

Most of all, the instrument should be able to record any spectral band in the visible and near-infrared range. Moreover, it should allow a properly chosen pair of two spectral bands to be recorded simultaneously. The coverage of each spectral band should be wide enough (> 10 Å) to include the whole portion of a chromospheric line, the nearby continua and a few photospheric lines, and the spectral resolving power should be high enough ($> 10^5$) to make the instrumental broadening negligible even in the narrowest solar lines. We set the goal for spatial resolution to $0.2''$ at the Hα line, which is just enough to reveal fine threads, but is not so high as $0.1''$, the diffraction-limited resolution of the 1.6 meter telescope. The field of view should be large enough to contain a significant number of recognizable features, say, $60'' \times 60''$. The temporal resolution is determined by the time interval between successive scans, which in turn depends on the width of the field of view covered by each scan. We require the time interval to be shorter than 30 s. Finally, we require the data to have signal-to-noise ratios higher than 10. As a measure of the signal, we uses the rms of the spatial variation of line center contrast, which is 0.1 typically in the quiet Sun. Then our requirement is that the noise at the center of a line should be smaller than 1 % of intensity. The preliminary analysis of the feasibility of the FISS was carried out by Ahn et al. (2008) with a focus on the prominence observations.

It is not easy to satisfy all the different requirements mentioned above and conflicts may naturally arise among them: especially between high temporal resolution requirement and high signal-to-noise ratio requirement, and between high temporal resolution requirement and the wide field of view requirement. Therefore it is unavoidable to make compromise in some cases. For example, we may have to increase the exposure time for high signal-to-noise ratio at the sacrifice of either temporal resolution or field of view.

3. Details of the Instrument

3.1. Pre-slit Parts

Figure 1 schematically shows the pres-slit optical layout for the FISS. These pre-slit parts determine the imaging capability of the instrument. A beam of sunlight is gathered by the

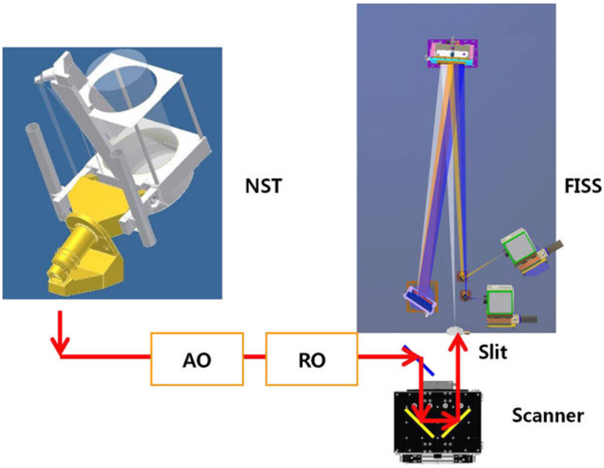

Figure 1 Schematic drawing of the optical layout of the instrument. The beam on the entrance slit is telecentric.

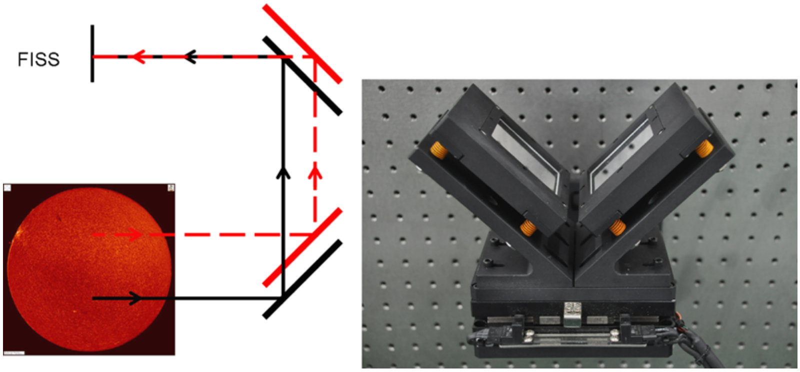

Figure 2 The optical layout (left) of the two-mirrored field scanner (right).

New Solar Telescope (NST), and is corrected for the troublesome seeing by the adaptive optics (AO). The beam is then relayed by the relay optics (RO) to the scanner and then to the entrance slit of the FISS where it becomes focused.

The NST is an off-axis Gregorian telescope with a parabolic primary mirror of $D = 1.6$ meter clear aperture. The AO currently consists of 76 wavefront sensor sub-apertures across the entrance pupil, and, when successfully operating, provides diffraction-limited images in the near IR (NIR). The next generation AO comprising 308 sub-apertures will enable diffraction-limited imaging in the visible as well. The RO consists of three folding mirrors and two lenses. It makes the beam incident on the slit not only be focused with $F = 26$, the same value as the FISS, but also be telecentric – the chief rays are set parallel to the optical axis.

3.2. Scanner

The field scanner is a device that shifts the incident beam across the slit. We do not use a commonly used scanner based on a tip-tilt mirror since it should be located at a pupil for the incident beam to have a telecentric configuration, which is a very difficult requirement in our case. Alternatively, we use a scanner of another type as depicted in Figure 2. In this type, the beam is shifted by a set of two mirrors that linearly moves in the direction across the slit. Note that a three-mirrored version of the Dove prism was previously used as a field scanner (Stolpe and Kneer, 1998), but a two-mirrored one is not. In this specific configuration, the two mirrors are set normal to each other, and the displacement of the beam becomes twice that of the scanner.

The manufactured field scanner consists of two flat mirrors mounted on an opto-mechanical grade linear motor made by the company Justek. The motor is controlled by a PMAC Mini board made by the Delta Tau company. The accurate control of this step-wise motion is realized by implementing the technique of proportional-integral-derivative (PID) gain control. This control can reduce the positional error within 1 µm, and finishes a displacement of one step (either 8 µm or 16 µm) typically within 70 ms.

The raster scan is realized by the simultaneous control of the linear motion of the scanner and the image acquisition of the cameras. The default mode is to have the scanner move step by step. It moves one step, stops, waits for each of the cameras to take one frame, and moves to the next step. It typically takes 0.1 s to proceed one step this way. The step size is set to the pixel size of the camera or the effective pixels of the resulting two-dimensional map of intensity to be of square shape. The detailed description of the field scanner is given by Ahn (2010).

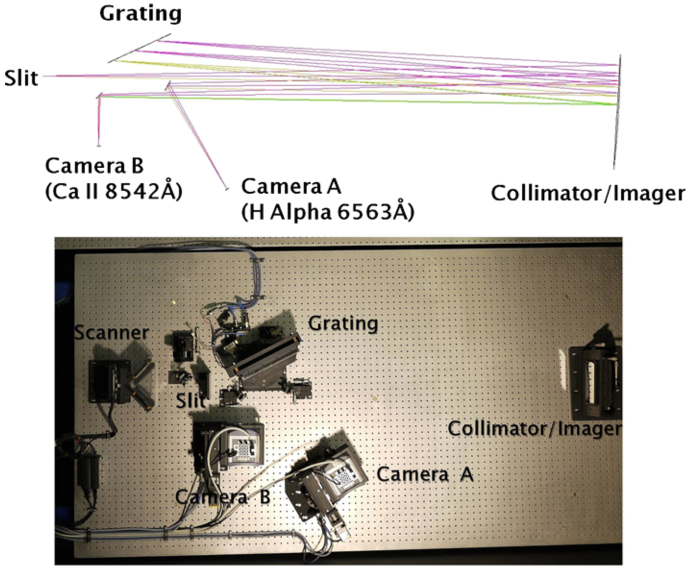

Figure 3 The optical layout (top) and the manufactured product (bottom) of the main body of the FISS. The distance between the slit and the collimator/imager is equal to the focal length of the collimator/mirror, 1500 mm.

3.3. Main Body

As is shown in Figure 3, the main body of the FISS consists of an entrance slit, a collimator/imager, an echelle grating, two broadband filters, and two cameras. The focused beam light enters the slit, becomes collimated by the collimator, gets spectrally dispersed by the grating, and then becomes focused by the imager. One spectral band is recorded on camera A, and another one, on camera B. The broadband interference filter mounted at the front of each camera transmits only the light in the spectral range of interest, removing overlapped light of other orders.

The beam is telecentric at the entrance slit, and forms a pupil at a point near the grating. To allow space for other optical components, the position of the grating was a little displaced from the pupil toward the collimator/imager. We find from the ray analysis that the effect of this deviation on the quality of imaging is negligible, and the spot diagrams are not sensitive to the precise position of the grating.

The slit has a width of $w = 32\ \mu\text{m}$ and a length of 20 mm. Currently the field of view along the slit is not determined by the slit, but by the detector chip which has a shorter length along the slit.

The mirror used as both the collimator and the imager is an off-axis paraboloid of 100 mm by 160 mm, which is a segment of a parabolic mirror of 300 mm aperture. Its focal length is $f = 1500$ mm. It was constructed in the Korea Research Institute of Standards and Science. The error in the radius of curvature is within 0.1 % and the rms error of the surface is less than $\lambda/40$. Note that the usage of the same mirror for both the collimator and the imager leads to transverse magnification of unity.

We adopted the Newport echelle grating of R2 ($\phi = 63.4°$) and $\sigma = 79$ groove/mm. This grating is mounted on a rotating table, and the grating angle can be set by controlling a stepping motor using a 6K controller manufactured by Parker. The resolution of the grating

Table 1 Incidence angles for the two lines of our interest in the two optical configurations with the grating parameters: 79 grooves/mm, $\phi = 63.4^\circ$. The parameters for the standard setup are emphasized in bold face.

Line (Å)		$\alpha - \beta = 0.93^\circ$			$\alpha - \beta = 1.92^\circ$		
		m	$\alpha - \phi$	B	m	$\alpha - \phi$	B
H I	**6562.8**	**34**	**−1.15**	**0.43**	34	−0.65	0.43
Ca II	**8542.1**	26	−1.65	0.42	**26**	**−1.14**	**0.43**

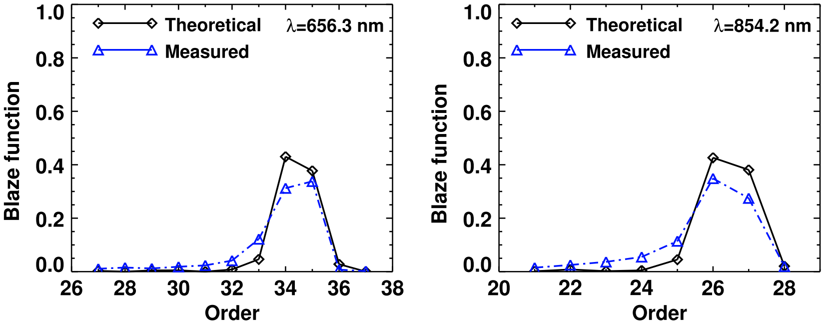

Figure 4 Theoretical and measured blaze functions for the Hα light (left) and Ca II 854.2 nm light (right), respectively. The measured values were normalized so as to make their summation be equal to the summation of all the theoretical values in each wavelength.

angle is 1.97″ per step. For the 34th order Hα light, this corresponds to the shift of 16 mÅ or one pixel on the detector.

The optical setup of each camera is determined by the value of $\theta \equiv \alpha - \beta$, the difference between incidence angle α and diffraction angle β. We choose $\theta = 0.93^\circ$ for camera A, and $\theta = 1.92^\circ$ for camera B. With wavelength λ given, α is to be determined from the grating equation,

$$\sin\alpha + \sin(\alpha - \theta) - \frac{m\lambda}{\sigma} = 0, \tag{1}$$

where the order m is an integer with which α maximizes the blaze function

$$B = \operatorname{sinc}^2\left(\frac{\pi\sigma\cos\phi}{\lambda}\big[\sin(\alpha - \phi) + \sin(\beta - \phi)\big]\right) \tag{2}$$

for a given ϕ. For the detailed knowledge on spectrographs including these equations, readers may refer to the textbook by Schroeder (2000). This blaze function becomes close to a maximum when $\alpha \approx \beta \approx \phi$, that is, in the quasi-Littrow configuration. With this choice, m is given by an integer that is close to $2\sigma\sin\phi/\lambda$.

Of our particular interest is the pair of the Hα line on camera A and the Ca II line at 8542 Å on camera B. The values calculated for these lines are listed in Table 1. Since this dual-band set is the most useful to our study, we regard it as the standard setup of the FISS. Regrettably, the blaze functions of this standard setup is much less than unity. This shortage arise from our choice of a commercially available grating item, Newport echelle grating: R2 that has the same values of σ and ϕ as specified above.

Figure 4 shows that the blaze functions measured as functions of order are close to theoretical values in the Hα band and in the Ca II 854.2 nm band, respectively. It is also found

Table 2 Parameters of the FISS instrumental setup. The coordinate x refers to the variation of position in the spectral direction on the detector, y, the one in the slit direction either on the detector or on the plane of sky, and z, the variation of the position across the slit on the plane of sky. Optional values are indicated inside the brackets.

Parameter	Variable	Value
Telescope aperture	D	1600 mm
Focal ratio of the beam	F	26
Slit width	w	32 [16] µm
Collimator/Image focal length	f	1500 mm
Grating groove density	$1/\sigma$	79 mm^{-1}
Grating blaze angle	ϕ	63.4°
Broadband filter (656.3 nm) bandwidth		10 nm
Broadband filter (854.2 nm) bandwidth		25 nm
Camera A deflection angle	θ	0.93°
Camera A format	$N_x \times N_y$	512 × 256 [512 × 512]
Camera A pixel size	$\delta x \times \delta y$	16 µm × 32 [16] µm
Camera A quantum efficiency at 656.3 nm	q	0.90
Camera B deflection angle	θ	1.92°
Camera B format	$N_x \times N_y$	502 × 251 [502 × 502]
Camera B pixel size	$\delta x \times \delta y$	16 µm × 32 [16] µm
Camera B quantum efficiency at 854.2 nm	q	0.35
Scanner step size	δz	32 [16] µm
Scanner stepping time		0.07 s
Scanner returning time		5 s

that the brightness of the 34th order Hα light is about 34 % of all the Hα light, and that of the 26th order Ca II 8542 Å light is about 38 %.

The order overlapping of different wavelengths is removed by using interference filters mounted in front of the CCD cameras. The full-width at half-maximum (FWHM) bandwidth of the filter for Hα is 10 nm, and the one for Ca II 8542 band is 25 nm. The peak transmissions of both filters are about 65 %.

Camera A used to record the Hα light is a back-illuminated (thin device)14-bit CCD camera DV 887 manufactured by the Andor company. Its quantum efficiency at the wavelength of the Hα light is about 90 %. This camera originally has 512 × 512 square pixels of 16 µm size. We usually bin the pixels by a factor of 1 × 2 so that the camera effectively has 512 × 256 pixels of 16 µm × 32 µm size. Since camera B recorded the Ca II line at 8542 Å is a front-illuminated (thick device) 14-bit camera DV885 made by the same company. The quantum efficiency of this camera at 8542 Å is about 35 %, being much lower than the above value. Note that we cannot use a thin device in this wavelength regime since it produces a destructive interference pattern. The original format of the camera is 1004×1002 square pixels of 8 µm size. We bin these pixels as well by a factor of 2 × 4 so that the camera effectively has 502 × 250 pixels of 16 µm × 32 µm size.

Table 2 summarizes the parameters of the FISS described so far. Note that the optional choice of the narrower slit and the finer samplings along the slit direction, and the smaller step size is to be made for higher spatial resolution observations.

3.4. System Control

A single computer controls the data acquisition by each of the two cameras, the focusing of each camera, the opening and closing of the slit cover, the rotation of the grating, and the linear motion of the scanner. The control software was developed using the Labwindows/CVI by National Instruments. In addition, the software displays data in different forms: spectrograms, raster images, line profiles, histograms of intensity, and so on. The software obviously provides the users with an interactive interface with which the users can set the operation mode, the CCD exposure times, the number of scans, scan time, step size, grating angle, and so on.

4. Data Acquisition and Processing

4.1. Data Acquisition

Three kinds of data are taken by the instrument: science data, dark/bias data, and flat/calibration data. The observing parameters for science data include the reference pixels of specified wavelengths, slit width, effective pixel size, integration times, step size, the total number of steps in each scan, and the total duration of each set of observations. Table 3 illustrates the parameters of a typical observation and the acquired data.

Dark/bias data are taken whenever the integration times are newly set. One hundred frames of dark/bias image are acquired by each camera with the same integration time as used for science data. The frames are averaged and only the average frame is finally stored

Table 3 Parameters of a typical observation and acquired data.

Observing parameters		
Slit width	w	32 µm
Camera A central wavelength	λ_c	656.28 nm
Camera A binning		1 × 2
Camera A exposure time	δt	30 ms
Camera B central wavelength	λ_c	854. 21 nm
Camera B binning		2 × 4
Camera B exposure time	δt	30 ms
Step size	δz	32 µm
Step number	N_z	100
Scan number		200
Data parameters		
Camera A data format		512 × 256 × 100
Camera A data pixel		1.9 pm × 0.16″ × 0.16″
Camera A data coverage		0.97 nm × 41″ × 16″
Camera B data format		502 × 250 × 100
Camera B data pixel		2.6 pm × 0.16″ × 0.16″
Camera B data coverage		1.31 nm × 40″ × 16″
Observing cadence	Δt	18 s
Total observing duration		1 h

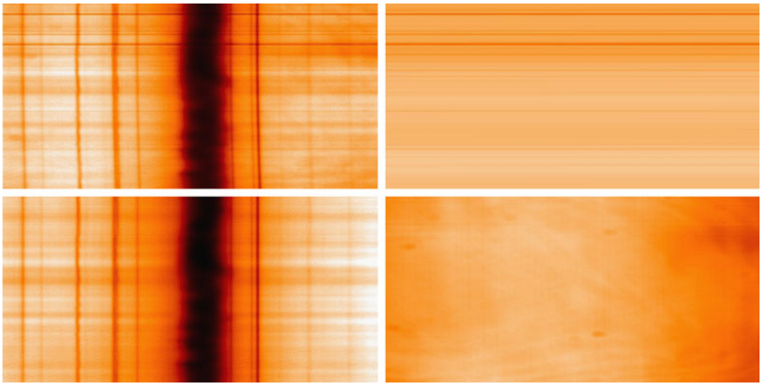

Figure 5 Left: examples of a raw Hα spectrogram (top) and its processed (bottom). Right: examples of the slit pattern (top) and the non-slit pattern (bottom) of the flat pattern. The data were taken on 23 July 2010.

into the hard disk of the computer. Subtracting this average frame does not lead to the amplification of noise that would arise when a single noisy frame of dark/bias image instead is used.

Flat/calibration data are taken more than once every observing day. A quiet region near the disk center is scanned for the purpose of flat fielding and other calibrations. The grating angle is set to ensure that spectral line of our interest is located at a specified position on the detector. The quiet region is scanned and as a result a total number of about 400 frames are acquired. These frames are averaged and only the average frame is kept for storage. Then the spectral line is displaced along the wavelength direction on the detector, and another average frame of the scan is prepared. This process is repeated seven times so that the positions of the spectral line well cover the wavelength dimension of the detector. The final products are two stored sets of seven averaged spectrograms for the two cameras. Note that one of the seven spectrograms in this flat/calibration data is used for the wavelength calibration of science data so that it should have the same spectral configuration as science data.

4.2. Flat Fielding

Correcting spectrograms for the non-uniform pattern of system response is a non-trivial part of data processing. We find it convenient to decompose the flat pattern into the slit pattern and the non-slit pattern. Figure 5 presents examples of the slit pattern and the non-slit pattern as well as a raw spectrogram.

The slit pattern originates from the non-uniformity of effective width of the slit, and is characterized by horizontal stripes. Sometimes these stripes may be tilted slightly from the horizontal direction. By taking into account this tilt, we determine this slit pattern from the median spectrogram constructed from the stored seven average spectrograms. Specifically, we obtain the two cuts of intensity along the slit direction, one at the left end of the detector, and the other at its right end. The displacement maximizing the cross-correlation of the two intensity cuts leads to the value of tilt, and the mean of the two cuts provides the one-dimensional slit pattern. By replicating this pattern in the wavelength direction with the tilt taken into account, we finally obtain the two-dimensional slit pattern. We divide the seven average spectrograms by this slit pattern and are ready to determine the non-slit pattern.

The non-slit pattern corresponds to the normal flat pattern of imaging observations. The flat pattern, in principle, is the image of a uniformly illuminating object. Since such an object does not exist on the sun, one may continuously change the field of view during the exposure so as to smooth out all the features. This simple technique, however, cannot be applicable to spectrograms, since spectral features are not smoothed out along the wavelength direction. Even though the positions of the lines on the detector are varied during the exposure, strong lines are hardly smoothed out.

Note that the proper determination of the flat pattern requires the information on its spatial variation in the two orthogonal directions: along the slit direction, that is, along the spatial direction, and across the slit direction, that is, along the spectral direction. The information on the variation of the flat pattern along the spatial direction comes from each of the seven spatially averaged spectrograms, because the spatially averaged spectrograms are supposed not to display any intrinsic spatial variation. The information along the spectral direction comes from the combination of all the spectrograms that have been relatively shifted one another along the spectral direction. To extract such information, we have developed an algorithm as described in Appendix A. This algorithm finds a pattern that optimally fits a model and is similar to the one developed by Chae (2004) for the application of filtergraph observations.

4.3. Distortion Correction

Top left panel of Figure 5 indicates that the spectral lines in the raw spectrogram are not perfectly straight, but slightly curved. This distortion results from the slight deviation of the incidence grating angle α from the value at the center of the grating, which in turn may be attributed to the slight inclination of the chief rays from the normal to the direction perpendicular to the slit. Fortunately, correcting for this distortion can be easily made only if the amount of displacement Δ_j is known. It can be determined from the cross-correlation of the j-th row spectrum and the reference spectrum that is taken from the central row. We suppress high frequency noise in Δ_j at each point by applying the piecewise quadratic polynomial fit to 30 data points surrounding the point of interest. Once Δ_j is determined, it is straightforward to correct for the distortion by shifting each row back by the amount of Δ_j. As a consequence, the spectral lines become vertically straightened.

4.4. Compression and Noise Reduction

We found the method of the principal component analysis (PCA) is very effective in reducing the amount of data without losing much physical information while suppressing noises. In the PCA, a spectral profile is expressed as a linear combination of all the principal components, and can be approximated by a linear combination of a small number of principal components. This PCA compression turns out to be successful especially when spectral profiles are similar to one another (Rees *et al.*, 2000), which is usually the case in solar observations. The details of the PCA compression used are described in Appendix B.

Let us illustrate how we have determined the set of eigenvectors and a suitable value of the compression factor N/n where N is the total number of data points in the spectral domain, and n is the number of coefficients retained in the PCA compression. Suppose a raster scan of a region is achieved by 100 steps of exposure on camera A of 512×256 pixels. It then follows that $N = 512$, and each scan contains a total of 100×256 independent spectral profiles of the Hα line. We randomly select 2000 spectral profiles to construct the covariance matrix. The eigenvalues and eigenvectors of this matrix are determined by applying an algorithm using Householder reductions and the QL method with implicit shifts. The eigenvalues and eigenvectors are placed in the descending order of eigenvalues.

Figure 6 Eigenvalues in the decreasing order (top), and the rms differences as a function of the number of terms retained in the compression (bottom).

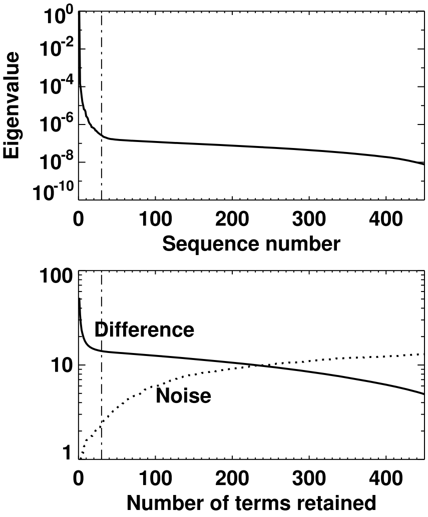

The top panel of Figure 6 shows the plots of eigenvalues normalized by the biggest one. It is clear from the figure that eigenvalues drop rapidly with sequence number $n < 50$ and then decrease slowly with n, with most eigenvalues being much smaller than the biggest one. We have compared a spectrogram with its compressed versions with different values of n, and have plotted the root-mean-squares of difference between the two as a function of n in the bottom panel of the figure.This difference measures the amount of information lost by the compression. It is likely that this lost information consists of more noise than statistically meaningful signal while the compressed data include more of such signal than noise. This means that the compression process naturally results in noise reduction.

We have empirically determined the standard noise in a set of data in the following way. If the sampling is fine enough to represent real features as smooth variations of intensity, pixel-to-pixel variations may be considered to mostly reflect noise. Base on this belief, we infer noise from a set of second-order finite differences each of which is calculated from three neighboring pixels. This method of estimate can be applied not only to raw data, but also to processed data.

The noise estimated in the continuum as a function of n is presented in the figure. Obviously, the smaller n is, the smaller the noise is, indicating that the compression reduces the noise. The noise in the uncompressed data is estimated to be 14 DN (data number). We choose 30 for the value of n for an optimal compression. This means that data are compressed by a factor of about 17. With this choice, the value of the rms difference is found to be about 14 DN, which is very close to the noise in the uncompressed data, and the noise is estimated to be about 1.9 DN. Therefore we conclude that the choice $n = 30$ is big enough for retaining most of non-noise features, and small enough for significantly reducing noise. A good thing is that the specific value of n is not critical to the behavior of data compression: the figure indicates that values of n in the range from 20 to 40 yields similar values of rms difference. Figure 7 illustrates the comparison of an uncompressed spectral profile and the one compressed with $n = 30$, and the profile of difference between them.

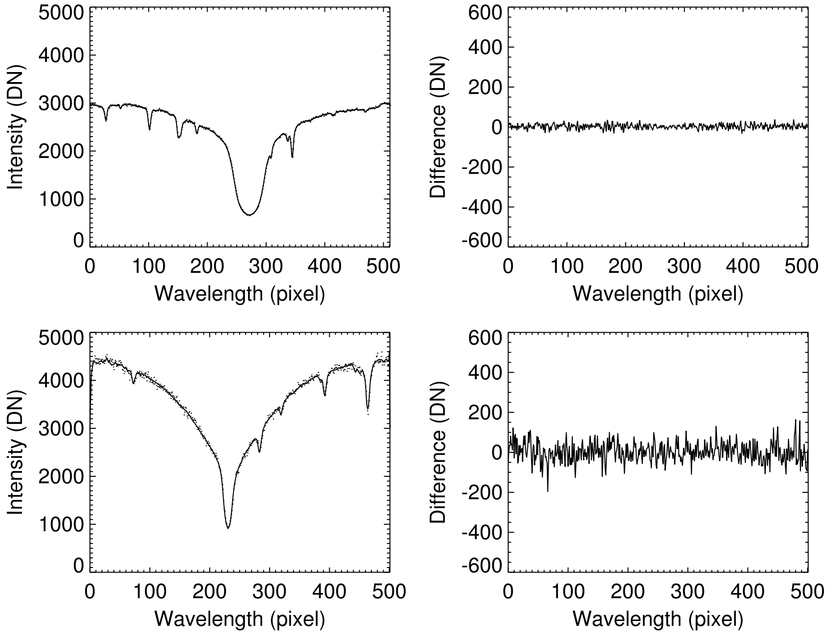

Figure 7 Left: the comparison of an compressed spectral profiles (solid) with the uncompressed ones (dots) for the Hα band and the Ca II 8542 band. Right: the profiles of difference between the two. The data were taken on 23 July 2010.

Table 4 Measured intensities and noises.

Parameter	Variable	Hα band	8542 band
Signal of continuum (measured)	S (DN)	2890	4210
Noise (uncompressed data)	N (DN)	14	46
Noise (compressed data)	N (DN)	2.8	8.3
Signal of line center (measured)	S (DN)	707	980
Signal of a 10 %-contrast feature (estimated)	S (DN)	71	98
Noise (uncompressed data)	N (DN)	7	28
Noise (compressed data)	N (DN)	1.1	4.3

5. Performance of the Instrument

5.1. Signal-to-Noise Ratio

Table 4 lists the values of light intensity and noise measured from the data. The amount of light detected by each pixel of the CCD camera is stored in unit of DN (data number). From the same set of data that is used for Figure 7, we found that the quiet Sun average of the continuum light in the Hα band is about 2890 DN, and that of the continuum in the Ca II 8542 band is about 4210 DN. We also estimated the standard noises from the uncompressed data and the PCA compressed data, respectively, using the method of second-order finite differences mentioned above. Since the detection of a chromospheric feature is

Table 5 Theoretical calculations of spectral resolution when the slit width is set to either 16 µm or 32 µm.

Parameter	Hα band	Ca II 8542 band	HeNe laser
Wavelength	6563 Å	8542 Å	6328 Å
Order	34	26	36
Detector size	19 mÅ	25 mÅ	15 mÅ
Detector coverage	9.7 Å	12.9 Å	7.8 Å
Grating resolution	19 mÅ	33 mÅ	18 mÅ
Spectral purity	18/36 m Å	24/48 mÅ	17/34 mÅ
Spectral resolution (net)	33/45 mÅ	48/64 mÅ	29/42 mÅ
Spectral resolving power	199 000/143 000	176 000/133 000	216 000/150 000

mainly through the core of these strong lines, we also determined intensities and noise at the line centers.

The values in Table 4 can be exploited to investigate the issue of signal-to-noise ratio. For instance, suppose we intend to study a feature which appears darker than the average Sun by 10 % at the central wavelength of the Hα line. The signal of this feature is then calculated to be $0.1 \times 707 = 71$ DN. Meanwhile the noise of the uncompressed data was measured to be 7 DN at the same wavelength, so that the resulting signal-to-noise ratio of the raw data turns out to be about 10. The PCA compression suppresses the noise significantly, which was found to be 1.1 DN. Therefore, the signal-to-noise ratio of the PCA compressed data has a higher value of 65. Meanwhile, in the Ca II 8542 Å line, the signal is 98 DN, and the measured noise is 28 DN, so that the signal-to-noise ratio is found to be 3.5. The PCA-compressed data are found to have a lower noise of 4.4 DN, leading to a higher signal-to-noise ratio of 22.

In Section 2.2, we mentioned that data should have signal-to-noise ratios higher than ten. Without compression, this requirement is barely achieved by spectral data of Hα line, but not by those of the Ca II 8542 Å line. Since the noise in the uncompressed data is dominated by photon noise, the low signal-to-noise ratio of the Ca II data is due to the small number of photons captured by camera B. We have investigated why the Ca II data have lower through-put than Hα data, and as a result, we found that there are two major reasons. First, the transmission of the telescope-spectrograph system is much lower in the Ca II band than in the Hα band, sine the system uses a total of 17 aluminum-coated reflecting surfaces. The ratio of the Ca II band transmission of these surfaces to the Hα band is 0.39. If all of these surfaces are silver-coated, the transmission of the system will increase by a factor of 2.9 in the Hα band, and 7.6 in the Ca II band. Another reason is obviously at the lower quantum efficiency of the front-illuminated CCD camera B, 0.35, which is much lower than that of the back-illuminated CCD camera B, 0.90.

5.2. Spectral Resolution and Spatial Resolution from a Lab Test

Table 5 presents how we calculated theoretical values of spectral resolution of the spectrograph at a few wavelengths. At the wavelength of 6328 Å, for example, the choice of the 16 µm slit leads to the spectral purity of 17 mÅ and the width of the illuminated part of the grating, to the grating resolution of 17 mÅ. The combined effect of these smearing factors as well as the finite size of a pixel, 15 mÅ, results in the theoretical net spectral resolution of 39 mÅ and the corresponding spectral power of 216 000 at the wavelength of 6328 Å.

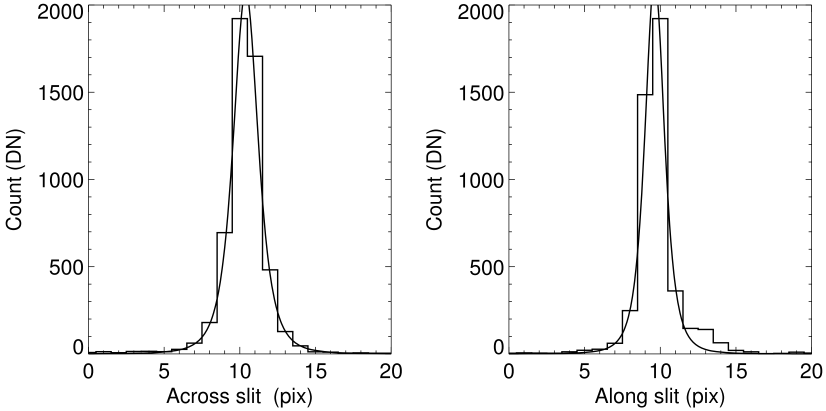

Figure 8 The spectral profile and spatial profiles of the spectral image of a monochromatic point source (laser source). The solid curves represent the model functions of the form $\sim 1/(((x - x_0)/a)^2 + 1)^2$.

We measured the spectral resolution and spatial resolution from a lab test using a HeNe laser source of monochromatic light at 6328 Å. The scanner was not operating this time, and the slit was set to 16 µm width. Figure 8 shows the spectral profile of the 36th order image of the source. The FWHM of the spectral profile is found to be about 2.2 pixels. With the use of the dispersion 15 mÅ/pixel at this wavelength, this value leads to the empirically determined spectral resolution of 33 mÅ and the resolving power of 1.92×10^5. These values are not much different from the values, 29 mÅ and 2.16×10^5 that we theoretically calculated.

Figure 8 also shows that the spatial profile of the point-like source has a small value of FWHM: 1.8 pixel. Since the size of a pixel is 16 µm or $0.08''$, the spatial resolution of the instrument is about $0.14''$, which is a measure of the performance of the imaging along the slit, and satisfactorily fulfills the requirement we set. Note that this value of spatial resolution depends on the optical setup, but neither on the performance of the scanner nor on the atmospheric seeing since it came from a lab test without using the scanner.

5.3. Imaging Capability of the Scanner

We examined the imaging capability of the scanner by taking the image of a resolution panel located at a focal position between the AO and the relay optics. The spatial resolution of this image is determined by the performance of the scanner, the optics of the combined system of the relay optics and the spectrograph, but not by the atmospheric seeing. Note that the vibration of the scanner may result in the degradation of image quality as the atmospheric seeing does; high frequency vibration may deteriorate the spatial resolution along the slit direction and low frequency vibration may introduce irregularity in the constructed raster scan image across the slit direction.

By analyzing the gradients of the blurred edges in the image of the resolution pane, we found that during the nominal operation of the scanner the FWHM *along* the slit has a value around the average 2.9 pixels (46 µm or $0.23''$), which is bigger than the value obtained above with the scanner being off. On the other hand, the FWHM *across* the slit was found to have an average value of 2.2 pixels (35 µm or $0.18''$). The stability of the scanning has been examined using a time series of raster images of a small quiet region constructed from the data taken by repeated scans. The cadence of the scans was fast enough to preserve the pattern of granulation. The cross-correlation analysis of two successive images taken at the

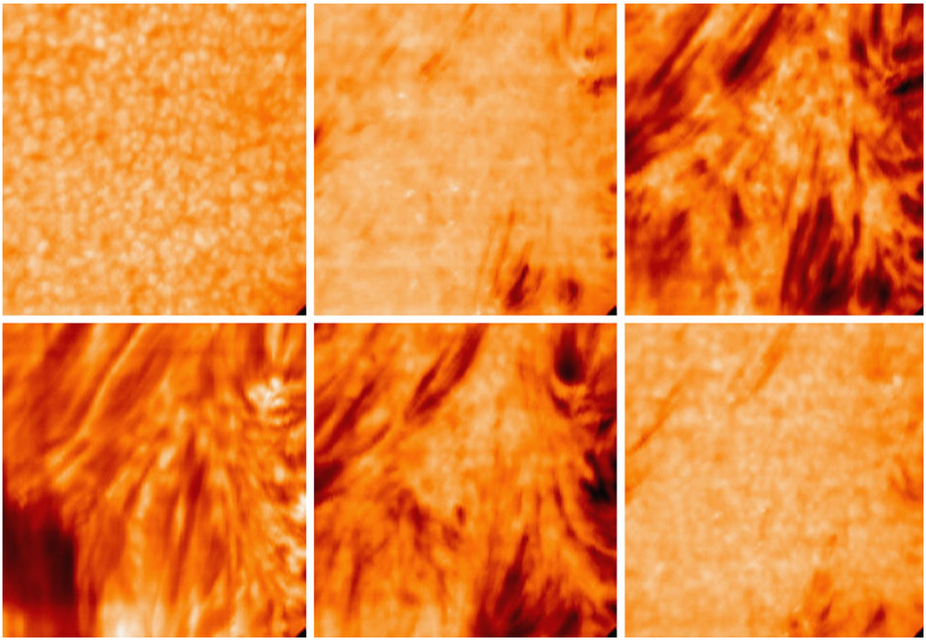

Figure 9 Raster images of a quiet region constructed at wavelengths −4.0, −0.8, −0.5, 0, 0.5, and 0.8 Å of Hα from top left to bottom right. The field of view is $38''$ by $41''$, and the spatial resolution is estimated to be $0.6''$. The observation date was 1 July 2011.

near-continuum indicates that they cover the same field of view within the uncertainty of one step size ($0.16''$), indicating that the scanning of the instrument is stably repeatable.

5.4. Net Spatial Resolution of Real Observations

Generally speaking, the net spatial resolution as well as the performance of the scanning strongly depends on the atmospheric seeing condition, even when the AO operates. This is because the performance of the AO is not perfect and is sensitive to the availability of high contrast features that in turn depends on the seeing.

The images in Figures 9 and 10 represent the best ones obtained so far, one from a quiet region, and the other from an active region. They can be used to infer the net spatial resolution of the instrument that includes the effect of seeing. It is clear from the images that granulation is well identified in Hα images. This suggests that the spatial resolution of Hα observations is better than $1''$. Identifying smallest bright structures, usually at the wing wavelengths, and measuring their widths along the slit direction, we obtained the estimates of spatial resolution in the these two cases, which are $0.6''$ and $0.7''$, respectively.

On the other hand, the Ca II 8542 observations shown in Figure 10 have poorer spatial resolution of $1.2''$ than the Hα observations that were simultaneously done. The dependence of seeing on wavelength cannot explain for this discrepancy, and recently we came to realize that the focusing of early (2010 and 2011) observations had not been optimized for the Ca II band. The two lens in the relay optics are subject to chromatic abberation so that there exists a small difference in the focal position between 6563Å and 8542 Å lights. Unless the lens positions are well adjusted so that the slit becomes located between the two focal

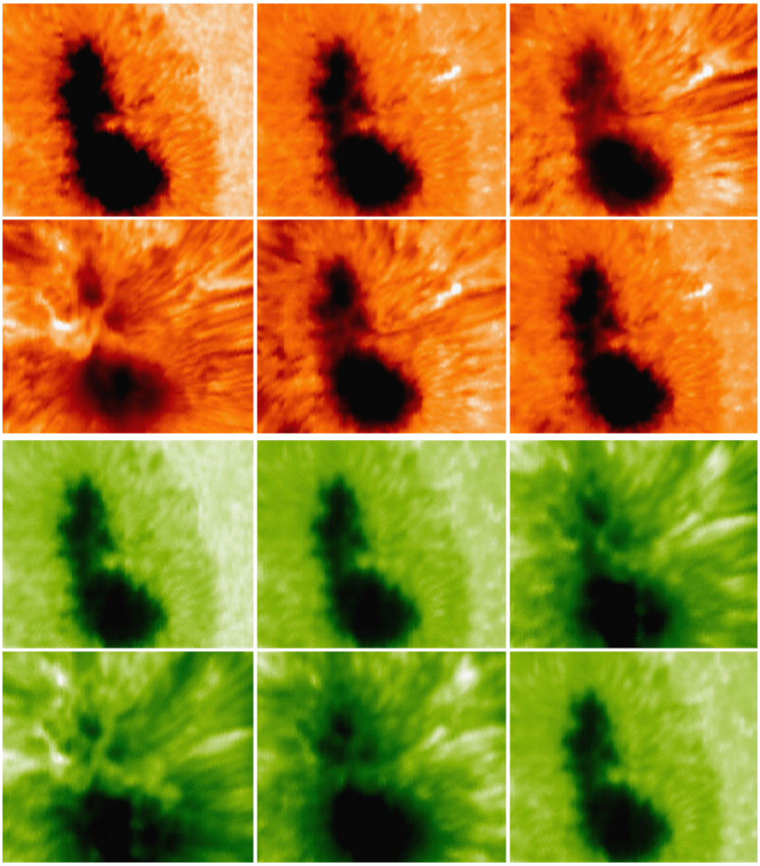

Figure 10 Top: Raster images of a quiet region constructed at wavelengths −4.0, −0.8, −0.5, 0, 0.5, and 0.8 Å of the Hα line from top left to bottom right. The field of view is 48″ by 41″, and the estimated spatial resolution is 0.7″. Bottom: Raster images of a quiet region constructed at wavelengths −4.0, −0.8, −0.3, 0, 0.3, and 0.8 Å of the Ca II 8542 line from top left to bottom right. The field of view is 48″ by 40″, and the spatial resolution is 1.2″. The data were taken on 4 August 2011.

positions, one bench becomes much out of focus even though the other bench is in focus. The chromatic abberation will be completely removed when the lenses are replaced by carefully designed achromatic ones.

5.5. Time Resolution

The number of steps in each scan determines time resolution and the width of the field of view. One step needs a total of 110 ms for the movement of the scanner (70 ms), and the exposure time (30 ms), and the spare time (10 ms). Since the readout of the cameras is done during the spare time and the scanner motion, it does not lengthen the cadence. The completion of 100 steps takes 11 s. Adding an extra time of 5 s required for the scanner to return to the origin, we finally obtain the time resolution of 16 s for successive scans each of which consisting of 100 steps. In this case, the width of the field of view is 16″. On the other hand, when the number of steps was 10, the time resolution was found to be as good as 2.1 s, and when the number of steps was 300, it was found to be as poor as 48 s.

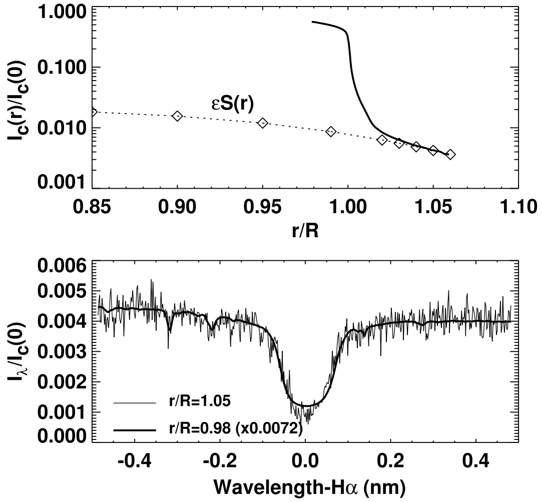

Figure 11 Top: profile of continuum intensity (solid curve) and the modeled scattered light integral (dotted curve with symbols). Bottom: Profile of the Hα line inside the limb (re-scaled by a factor of 0.0072) and the one outside the limb. The data were taken on 30 June 2010.

5.6. Stray Light

Two kinds of stray light affect the spectrograph observations: spatial stray light and spectral stray light (see Appendix C). The continuum intensity outside the solar limb is a measure of spatial stray light produced by the terrestrial atmosphere and the observing instrument. By analyzing the map of continuum intensity constructed from the spectrograms taken at the east limb on 30 June 2010, we have determined the spatial variation of the intensity across the limb as a function of angular distance from the center of the solar disk, as shown in the upper panel of Figure 11. We have modeled the scattered light integral $S(r)$ that measures the effect of large spread angle stray light by introducing a Gaussian spread function with a FWHM of $200''$ and as a result we found that the stray light fraction near disk center ϵ is about 0.027. Furthermore, the lower panel of Figure 11 supports our expectation that the effect of spatial stray light is uniform over wavelength, preserving the shape of the spectral profile. In fact, it is spectral stray light that affects it.

We estimated the fraction of spectral stray light ζ by comparing the observed spectral profile of the Hα line with the atlas of Wallace, Hinkle, and Livingston (2007). According to this atlas, the core-to-continuum intensity ratio of the Hα profile taken at the disk center of the quiet Sun is 0.16. In comparison, the core-to-continuum intensity of the average quiet Sun profile taken by the FISS is found to be 0.21. As a result, ζ is estimated to be 0.065.

6. Summary and Conclusion

We have described the design, specifics, data manipulation, and performance of the FISS. The instrument was designed to take high signal-to-noise ratio spectra of chromospheric features at high spatial resolution, high spectral resolution, and high temporal resolution, but it is not possible to meet all the requirements and it is necessary to compromise among different needs.

Figures 10 and 12 provide examples of data that are currently taken by the FISS, spectrograms that are in the original form (Figure 12) and raster images that come out of processing (Figures 10). The strength of the instrument is definitely in the capability of recording the

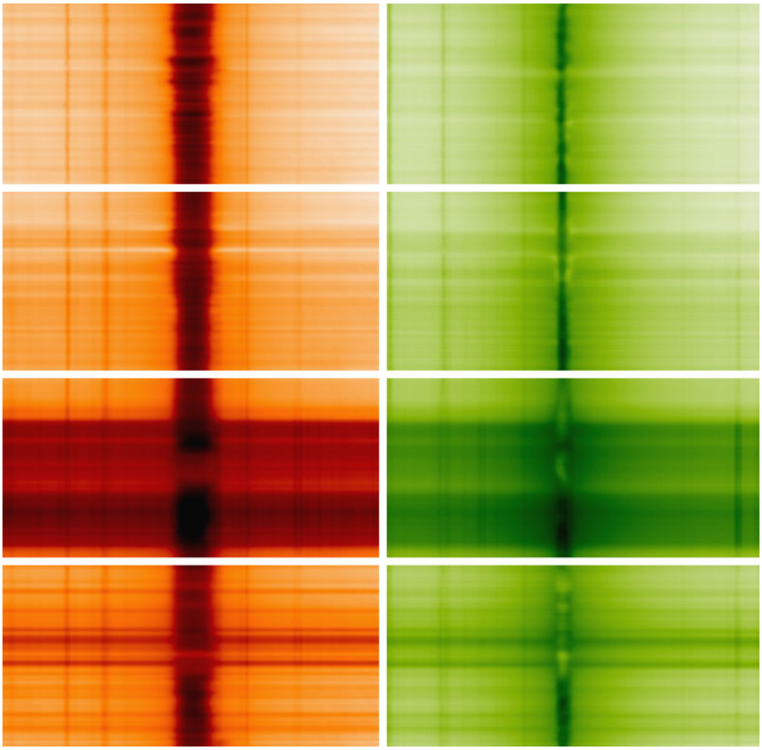

Figure 12 Examples of the pair of an Hα spectrogram and a Ca II 8542 spectrogram taken simultaneously at different locations of the active region shown in Figure 10.

two important spectral lines – Hα and Ca II 8542 Å line – exactly simultaneously. Both these lines are significantly affected by the presence of dense material in the chromosphere, but they reflect its thermal structure and dynamics in different ways. Specifically it is clear from Figure 12 that absorption structures are better reflected in the Hα line, and emission structures, better in the Ca II line.

Several important characteristics and the current performance of the instrument are summarized as follows:

i) The spectral coverage is big enough to include one strong absorption line – such as the Hα line and Ca II 8542 Å line – useful for the observation of the chromosphere and a few weaker lines useful for the observations of the photosphere.
ii) The spectral resolution is satisfactorily high. With the slit of 0.08″ width, the spectral resolving power is above 1.5×10^5. With a wider slit, the spectral resolution is a little degraded, but is still satisfactory.
iii) We found that the PCA (principal component analysis) compression can be implemented successfully. This kind of processing not only reduces the size of data to be stored by a factor of up to 20, but also suppresses noise significantly.
iv) We found that noise in the uncompressed data is dominated by photon noise. The signal-to-noise ratio of data is hence determined by the amount of light gathered by each pixel on the CCD camera.

v) The spatial resolution of the instrument without taking into account the effect of seeing, is estimated to be about 0.25″. On the other hand, the net spatial resolution including the effect of seeing and the AO is found to be 0.6″ or poorer.

We plan to improve the FISS in several stages. The first stage is to improve the quality of the Ca II data by replacing the lenses in the relay optics by achromatic ones that can precisely match the focal lengths of the Hα and Ca II benches. We will also increase the throughput of the system by replacing the grating with an optimal blaze angle, and aluminum-coated reflecting surfaces by silver-coated ones. The significant improvement in the spatial resolution will be made with the implementation of higher-order adaptive optics of 308 subapertures in the Coudé Lab of the telescope.

Acknowledgements We are grateful to the referee for a number of constructive comments. This work was supported by the National Research Foundation of Korea (KRF-2008-220-C00022) and by the Development of Korean Space Weather Center, a project of KASI.

Appendix A: Flat Fielding

Let us denote the index of a pixel along the wavelength direction by i and that along the slit direction, by j. An averaged spectrogram, s_{ij} should depend on i only, but not on j if the spatial average is ideally done so that we may write $s_{ij} = o_i$ where o_i is the one-dimensional spectrum of the average sun. Then the kth spectrogram a^k_{ij}, that is acquired by the camera with the spectrum being displaced by x_k from the reference spectrum along the wavelength direction can be mathematically modeled as:

$$a^k_{ij} = c_k s_{i-x_k,j} f_{ij} = c_k o_{i-x_k} f_{ij}, \tag{3}$$

where f_{ij} is the flat pattern we intend to determine, and c_k is the relative level of intensity. We find it necessary to modify this equation a little bit, for the spectral lines in the acquired spectrograms are not vertically straight, but slightly curved. This distortion may be considered as a manifestation of horizontal displacement of spectrum depending on the position along the slit, which we denote by Δ_j. Taking into account this distortion, we modify the above equation into

$$a^k_{ij} = c_k o_{i-\Delta_j-x_k} f_{ij}, \tag{4}$$

or into its logarithmic form,

$$A^k_{ij} = C_k + O_{i-\Delta_j-x_k} + F_{ij}. \tag{5}$$

For given A^k_{ij}, x_k, and Δ_j, maximizing

$$H = \sum_{ijk} \left(C_k + O_{i-\Delta_j-x_k} + F_{ij} - A^k_{ij}\right)^2 w(i - \Delta_j - x_k) \tag{6}$$

and

$$K = \sum_{ijk} \left(C_k + O_i + F_{i+\Delta_j+x_k,j} - A^k_{i+\Delta_k+x_k,j}\right)^2 w(i + \Delta_j + x_k) \tag{7}$$

we obtain the iterative formulas: for F_{ij}

$$\Delta F_{ij} \approx -\frac{\sum_k (C_k + O_{i-\Delta_j-x_k} + F_{ij} - A^k_{ij}) w(i - \Delta_j - x_k)}{\sum_k w(i - \Delta_j - x_k)}, \tag{8}$$

for C_k

$$\Delta C_k = -\frac{\sum_{ij}(C_k + O_{i-\Delta_j - x_k} + F_{ij} - A^k_{ij}) w(i - \Delta_j - x_k)}{\sum_{ij} w(i - \Delta_j - x_k)}, \tag{9}$$

and for O_i

$$\Delta O_i \approx -\frac{\sum_{jk}(C_k + O_i + F_{i+\Delta_j + x_k, j} - A^k_{i+\Delta_k + x_k, j})}{\sum_{jk} w(i + \Delta_j + x_k)}. \tag{10}$$

Note that $w(x)$ and $v(y)$ are functions that have values of either unity or zero depending on whether x and y are inside the corresponding index ranges, respectively. These expressions for the iteration are similar to those given by Chae (2004) so we do not go into further details.

Appendix B: Compression

Generally speaking an arbitrary vector I_i of N elements ($i = 1, \dots, N$) can be written as a linear combination of a set of N orthonormal vectors s_i^k ($k = 1, \dots, N$). Specifically we choose the form

$$I_i = \bar{I} \sum_{k=1}^{N} c_k s_i^k, \tag{11}$$

where $\bar{I}$ is the average intensity. The coefficient c_k is determined from I_i:

$$c_k = \sum_{i=1}^{N} \frac{I_i}{\bar{I}} s_i^k. \tag{12}$$

If s_i^k can be placed in descending order of statistical significance, we can reduce the number of coefficients to be kept to $n < N$ while retaining most physical information:

$$I_i \approx \bar{I} \sum_{k=1}^{n} c_k s_i^k. \tag{13}$$

Data are thus compressed by a factor of N/n.

The set of basis vectors s_i^k is constructed from the database of model profiles, J_i^l ($l = 1, \dots, M$), that well represent spectral profiles to be analyzed. By referring to Rees *et al.* (2000), we define a symmetric covariance matrix

$$A_{ij} = \sum_{l=1}^{M} \frac{J_i^l}{\bar{J}^l} \frac{J_j^l}{\bar{J}^l} \tag{14}$$

and identify its kth eigenvector with the kth basis vector s_i^k while the eigenvectors are sorted in the descending order of the associated eigenvectors. Note that the statistical significance of s_i^k is measured by its associated eigenvalue λ_k.

Appendix C: Stray Light Model

We model the effect of spatial stray (large-angle spread) light on the data using the equation

$$\frac{I_c^{\text{obs}}(\mathbf{r})}{I_c^{\text{obs}}(0)} = (1 - \epsilon)\frac{I_c(\mathbf{r})}{I_c(0)} + \epsilon S(\mathbf{r}) \tag{15}$$

and that of spectral stray (large-wavelength spread) light using the equation

$$\frac{I_\lambda^{\rm obs}(\mathbf{r})}{I_c^{\rm obs}(\mathbf{r})} = (1-\zeta)\frac{I_\lambda(\mathbf{r})}{I_c(\mathbf{r})} + \zeta V_\lambda, \tag{16}$$

where $I_c^{\rm obs}(\mathbf{r})$ and $I_c^{\rm obs}(0)$ are the observed intensities of the continuum at an arbitrary position $\mathbf{r}$ and the disk center, respectively, and $I_\lambda^{\rm obs}(\mathbf{r})$ and $I_\lambda^{\rm obs}(0)$ refer to those at an arbitrary wavelength λ. The intrinsic intensities $I_c(\mathbf{r})$, $I_c(0)$, $I_\lambda(\mathbf{r})$, and $I_\lambda(0)$ are defined in the same way.

In our model, the effects of spatial stray light and spectral stray light on a spectrogram are independent from each other; the spatial stray light affects the level of intensity equally over different wavelengths, and the spectral stray light affects the shape of each spectrum. The spatial stray light integral $S(\mathbf{r})$ is a normalized function slowly varying over the position $\mathbf{r}$, but may be approximated to be equal to a constant value, 1, near the disk center. In a similar way, the spectral stray light integral V_λ is a normalized function slowing varying over wavelength λ, but may be approximated to be equal to a constant value, 1. Therefore, the correction of stray light in disk observations can be done if two parameters, the fraction of spatial stray light ϵ and the fraction of spectral stray light ζ, are known.

References

Ahn, K.: 2010, Development of New Astronomical Instruments for High Resolution Solar Observations. Ph.D. thesis, Seoul National University.

Ahn, K., Chae, J., Park, H.-M., Nah, J., Park, Y.-D., Jang, B.-H., Moon, Y.-J.: 2008, *J. Korean Astron. Soc.* **41**, 39.

Beckers, J.M.: 1964, A Study of the Fine Structures in the Solar Chromosphere. Ph.D. thesis, Utrecht University.

Cao, W., Gorceix, N., Coulter, R., Ahn, K., Rimmele, T.R., Goode, P.R.: 2010, *Astron. Nachr.* **331**, 636.

Cavallini, F.: 2006, *Solar Phys.* **236**, 415.

Chae, J.: 2004, *Solar Phys.* **221**, 1.

Chae, J., Park, Y.-D., Park, H.-M.: 2006, *Solar Phys.* **234**, 115.

de Pontieu, B., McIntosh, S., Hansteen, V.H., Carlsson, M., Schrijver, C.J., Tarbell, I.M., *et al.*: 2007, *Publ. Astron. Soc. Japan* **59**, 655.

Goode, P.R., Denker, C.J., Didkovsky, L.I., Kuhn, J.R., Wang, H.: 2003, *J. Korean Astron. Soc.* **36**, S125.

Goode, P.R., Coulter, R., Gorceix, N., Yurchyshyn, V., Cao, W.: 2010, *Astron. Nachr.* **331**, 620.

Hanaoka, Y.: 2003, In: Keil, S.L., Avakyan, S.V. (eds.) *Innovative Telescopes and Instrumentation for Solar Astrophysics*, *Proc. SPIE* **4853**, 584.

Judge, P.: 2006, In: Leibacher, J., Stein, R.F., Uitenbroek, H. (eds.) *Solar MHD Theory and Observations: A High Spatial Resolution Perspective*, *ASP Conf. Ser.* **354**, 259.

Langangen, Ø., De Pontieu, B., Carlsson, M., Hansteen, V.H., Cauzzi, G., Reardon, K.: 2008, *Astrophys. J.* **679**, L167.

Nah, J.-K., Chae, J.-C., Park, Y.-D., Park, H.-M., Jang, B.-H., Ahn, K.-S.: *et al.*: 2011, *Publ. Korean Astron. Soc.* **26**, 45.

Park, H.: 2011, Development of Fast Imaging Solar Spectrograph and Observation of the Solar Chromosphere. Ph.D. thesis, Chungnam National University.

Reardon, K.P., Uitenbroek, H., Cauzzi, G.: 2009, *Astron. Astrophys.* **500**, 1239.

Rees, D.E., López Aristle, A., Thatcher, J., Semel, M.: 2000, *Astron. Astrophys.* **355**, 759.

Rutten, R.: 2006, In: Leibacher, J., Stein, R.F., Uitenbroek, H. (eds.) *Solar MHD Theory and Observations: A High Spatial Resolution Perspective*, *ASP Conf. Ser.* **354**, 276.

Schroeder, D.J.: 2000, *Astronomical Optics*, 2nd edn., Academic Press, San Diego.

Shibata, K., Nakamura, T., Matsumoto, T., Otsuji, K., Okamoto, T.J., Nishizuka, N., *et al.*: 2007, *Science* **318**, 1591.

Stolpe, F., Kneer, F.: 1998, *Astron. Astrophys. Suppl.* **131**, 181.

Tziotziou, K.: 2007, In: Heinzel, P., Dorotovič, I., Rutten, R.J. (eds.) *The Physics of Chromospheric Plasmas*, *ASP Conf. Ser.* **368**, 217.

Wallace, L., Hinkle, K., Livingston, W.: 2007, *An Atlas of the Spectrum of the Solar Photosphere from 13,500 to 33,980 cm*$^{-1}$ (*2942 to 7405* Å). National Solar Observatory.